crystals

MDPI

Article

First-Principle Study on Correlate Structural, Electronic and Optical Properties of Ce-Doped $BaTiO_3$

Haojie Yue [1], Kailing Fang [1], Tiantian Chen [1], Qinfang Jing [1], Kun Guo [1,*], Zhiyong Liu [1], Bing Xie [1], Pu Mao [1], Jinshan Lu [1], Francis Eng Hock Tay [2], Ivan Tan [3] and Kui Yao [3]

[1] School of Materials Science and Engineering, Nanchang Hangkong University, Nanchang 330063, China
[2] Department of Mechanical Engineering, National University of Singapore, 9 Engineering Drive 1, Singapore 117575, Singapore
[3] Institute of Materials Research and Engineering, A*STAR (Agency for Science, Technology and Research), 2 Fusionopolis Way, Innovis, Singapore 138634, Singapore
* Correspondence: guokun@nchu.edu.cn

Abstract: The structural, electronic, and optical properties of pure and Ce-doped $BaTiO_3$ were investigated based on first-principle calculation. Here, we concentrate on understanding the effect of the substitution of Ce for Ba and Ti sites in the equilibrium lattice parameters, DOS, electronic band structure, and optical performance of the materials. The crystal structures with a 12.5% doping ratio at different sites were constructed by superseding an atom of Ba (or Ti) site with a Ce atom and investigating the optimized crystal structure parameters. The substitution of Ce leads to a reduction in the band gap by inducing the movement of the conduction band minimum (CBM) and valence band maximum (VBM). The reduction in the band gap has been shown to be beneficial in increasing electrical conductivity. The density of states of the materials was calculated to gain insight into the valence band, conduction band, and contribution of each orbital to the total density of states in the electronic structure. The charge density, Mulliken charges, and bond overlap populations of pristine and Ce-doped $BaTiO_3$ were calculated to understand the nature of chemical bonds before and after doping. In addition, the optical properties of the materials were calculated, and the substitution of Ce for Ba site increased the static dielectric constant. In contrast, it decreased when Ce was doped into the Ti site. The substitution of Ce for different sites reduced the reflectivity of the material, while the transparency of the materials before and after doping was almost the same. The materials were transparent to incident light when the photon energy was below 10 eV, whereas opacity was in the ultraviolet range of 10–13 eV and beyond 20 eV. The theoretical calculation of different properties provides a new idea for the theoretical study of the $BaTiO_3$-based system.

Keywords: first-principle; $BaTiO_3$ lead-free ceramic; perovskite structure; electronic property; optical property

Citation: Yue, H.; Fang, K.; Chen, T.; Jing, Q.; Guo, K.; Liu, Z.; Xie, B.; Mao, P.; Lu, J.; Tay, F.E.H.; et al. First-Principle Study on Correlate Structural, Electronic and Optical Properties of Ce-Doped $BaTiO_3$. *Crystals* **2023**, *13*, 255. https://doi.org/10.3390/cryst13020255

Academic Editors: Luisa De Marco, Jinyan Zhao, Zenghui Liu and Ting Zheng

Received: 14 December 2022
Revised: 28 January 2023
Accepted: 30 January 2023
Published: 1 February 2023

1. Introduction

With the advent of Industry 4.0, there will be a strong demand for numerous functional devices, such as sensors, microactuators, and ultrasonic transducers, which utilize piezoelectric ceramics with excellent and reliable properties [1–7]. Lead-based piezoelectric materials, such as $Pb(Zr, Ti)O_3$, dominate the commercial market owing to their superior piezoelectric performance and temperature stability. However, lead-based piezoelectric materials bring severe environmental concerns because of the toxic lead components. Thus, developing lead-free piezoelectric materials with excellent performance has always been an essential topic. The $BaTiO_3$-based system is one of the most extensively investigated lead-free piezoelectric material systems. The Curie temperature (T_C) of $BaTiO_3$ is ~120 °C, and some ion doping even lowers the T_C of $BaTiO_3$-based ceramics to near ambient temperature [8–11]. In addition, due to the excellent dielectric and piezoelectric and ferroelectric

performance at room temperature, $BaTiO_3$-based ceramics are widely applied for capacitors and promising for electro-optical applications.

When the temperature is below 120 °C, the Ti^{4+} ions located in the body center of the crystal cell move close to a certain vertex of the surrounding oxygen octahedron, resulting in the entire crystal structure gradually changing from cubic to tetragonal. However, $BaTiO_3$ with the tetragonal structure is only stable when the temperature range is between 5 °C and 120 °C. As the temperature continues to decrease, a transition of crystal structure from tetragonal to orthogonal will occur [12,13]. Due to the practical restrictions, various chemical dopants have been applied to enhance the properties of $BaTiO_3$ ceramics. On the one hand, doping causes a change of T_C in $BaTiO_3$, which can be explained straightforwardly by ion-size effects and modifications to the tolerance factor [14–16]. On the other hand, some doping can significantly increase the conductivity of $BaTiO_3$, which can be attributed to the donor electron compensation effect [17]. In particular, rare-earth elements have become effective dopants due to their strong electronic charges and large ionic radius $BaTiO_3$ is often doped with rare-earth elements to improve mechanical and electrical properties. Researchers have conducted numerous experimental studies on the mechanism and physicochemical properties of $BaTiO_3$-based systems by various dopants. Some efforts have been made to prepare Ce-doped $BaTiO_3$ ceramic powders using the sol-gel method. High dielectric constant and low dielectric loss were achieved at the Curie temperature of 22 °C [18]. $(Ba_{1-x}Ce_x)TiO_3$ and $Ba(Ti_{1-y}Ce_y)O_3$ ceramic powders, fabricated by the liquid mix method, were investigated for their high-temperature equilibrium electrical conductivity in terms of oxygen partial pressure, $P(O_2)$, and composition [19]. With the increasing content of the Ce element, the Tc of $BaCe_xTi_{1-x}O_3$ ceramics decreased and a ferroelectric relaxation transition occurred [20]. However, the theoretical calculation studies on the effects of rare earth doping into $BaTiO_3$ are insufficient.

This paper demonstrated a systematic analysis of the structural, electronic, and optical properties of Ce-doped $BaTiO_3$ based on the first-principle method. In order to further understand the mechanism of $BaTiO_3$ and the effects of different sites doping on its performance, theoretical calculations were performed for both Ba-site and Ti-site doping. The effects of Ce doping on the crystal structures and electronic and optical properties of $BaTiO_3$ are presented in detail.

2. Computational Details

The simulation calculations were based on density function theory (DFT) using the Cambridge Serial Total Energy Package (CASTEP). The Ultrasoft pseudopotential (UPP) [21] generalized gradient approximation (GGA) was adopted to deal with the interaction between ions and electrons, and Perdew–Burke–Ernzerhof (PBE) was to cope with the exchange-correlation function [22–24]. The Hubbard energy U = 4 eV for Ti 3d orbitals and U = 5 eV for Ce 4f orbitals were applied to deal with the on-site Coulomb interaction and describe the exchange-correlation potential [25–28]. The cutoff energy was set to 580 eV for $BaTiO_3$ and Ce-doped $BaTiO_3$. The minimum energy tolerance was 10^{-6} eV per atom and the force tolerance was 2 meV/Å. To investigate the irreducible Brillion zone (BZ), Monkhorst-pack grids of $7 \times 7 \times 7$ and $4 \times 4 \times 4$ were implemented for pure $BaTiO_3$ and Ce-doped $BaTiO_3$, respectively [29,30].

The tetragonal unit cell of pure $BaTiO_3$ belongs to the space group P4mm, containing 5 atoms. For Ce-doped $BaTiO_3$, Considering the practicability and cost of calculation, a model with 40 atoms was constructed based on a $2 \times 2 \times 2$ $BaTiO_3$ supercell. The crystal structures with a 12.5% doping ratio at different sites have been constructed by superseding an atom of the Ba (or Ti) site with a Ce atom. Due to the symmetry of the crystal structure and atomic equivalence, there is only one model for one-eighth of Ba or Ti sites to be replaced by Ce atoms. Correspondingly, the concentrations are $Ba_{0.875}Ce_{0.125}TiO_3$ for substituting the Ba site and $BaTi_{0.875}Ce_{0.125}O_3$ for substituting the Ti site. As the valence electrons play a decisive role in the physicochemical properties of materials, only

the valence electrons were considered in these calculations. The atomic valence electrons involved in these materials are as follows

Ba: $6s^2$

Ti: $3d^2$ $4s^2$

O: $2S^2$ $2P^4$

Ce:$4f^1$ $5d^1$ $6s^2$

The valency of cerium considered here was +3 and +4 when the cerium ion was substituted for Ba^{2+} sites or Ti^{4+} sites, respectively. One measure of the stability of a structure is the tolerance factor, which may be computed from

$$t = \frac{r_0 + r_A}{\sqrt{2}(r_0 + r_B)} \quad (1)$$

where r_A and r_B are the ionic radius of A and B sites, respectively, whereas r_0 is the ionic radius of oxygen. For stable perovskite structure, the tolerance factor is considered in the range of $0.85 < t < 1.10$, and the high symmetry cubic structure value corresponds to $t = 1.00$. The tetragonal symmetry of $BaTiO_3$ has a tolerance factor of 1.06. When the tolerance factor t deviates from this range, the perovskite crystal structure will be distorted due to the tilt of the BO_6 octahedron, inducing a crystal structure transition to a non-perovskite structure [31].

3. Result and Discussion

3.1. Geometry Optimization

As presented in Table 1, the optimized lattice parameters and average bond length of pure $BaTiO_3$ and Ce-doped $BaTiO_3$ were calculated. Meanwhile, the estimated values and the experimental results were compared. The computed lattice parameter values for pure $BaTiO_3$ corresponded well with the previous theoretical results but were significantly larger than the experimental result. Due to there being a wrong self-interaction in the GGA method, the interaction between the electron and itself is improper, the delocalization of the electron is enhanced, and the lattice parameters are larger than the real system. For Ce-doped $BaTiO_3$, the lattice parameters were found to be slightly changed at both the A and B sites, which were relatively compatible with the experimental results published in the literature [19]. Figure 1 shows the crystal structures of pure $BaTiO_3$ and Ce-doped $BaTiO_3$ at different sites. For $Ba_{0.875}Ce_{0.125}TiO_3$, the lattice parameter a is somewhat larger than that of pure $BaTiO_3$, while the lattice parameter c and cell volume (V) are marginally smaller. In the case of $BaTi_{0.875}Ce_{0.125}O_3$, the parameters a, c, and volume (V) are all greater than that of pristine perovskite. The Ti-O bond length was determined by the octahedral sites occupied by Ti atoms, whereas the Ba-O bond length was associated with the dodecahedral sites occupied by Ba atoms. The assessed Ba-O and Ti-O bond lengths of the optimized pure $BaTiO_3$ were 2.823 Å and 2.017 Å, respectively. The results were in good agreement with previous theoretical findings and relatively consistent with the experimental results [32–34]. For the incorporation of the Ce element, both the Ti-O and Ba-O bond lengths significantly increased due to the lattice distortion. It can be concluded that there is a long-range effect of Ce doping on the perovskite, resulting in a modification of the interatomic bond lengths.

Table 1. Optimized lattice parameters, cell volume, and average bond length for pristine and Ce-doped $BaTiO_3$.

Compound	Method	a (Å)	c (Å)	V (Å^3)	Ba-O(Å)	Ti-O (Å)	Ce-O (Å)
$BaTiO_3$	GGA-PBE	4.023	4.161	67.344	2.823	2.017	
		4.007 [32]	4.186 [32]	67.211 [32]			
		3.967 [33]	4.232 [33]	66.599 [33]			
	Experiment	4.000 [34]	4.024 [34]	64.384 [34]			
$Ba_{0.875}Ce_{0.125}TiO_3$	GGA-PBE	4.033	4.063	66.085	2.856	2.024	2.619
$BaTi_{0.875}Ce_{0.125}O_3$		4.079	4.240	70.546	2.854	2.078	2.258

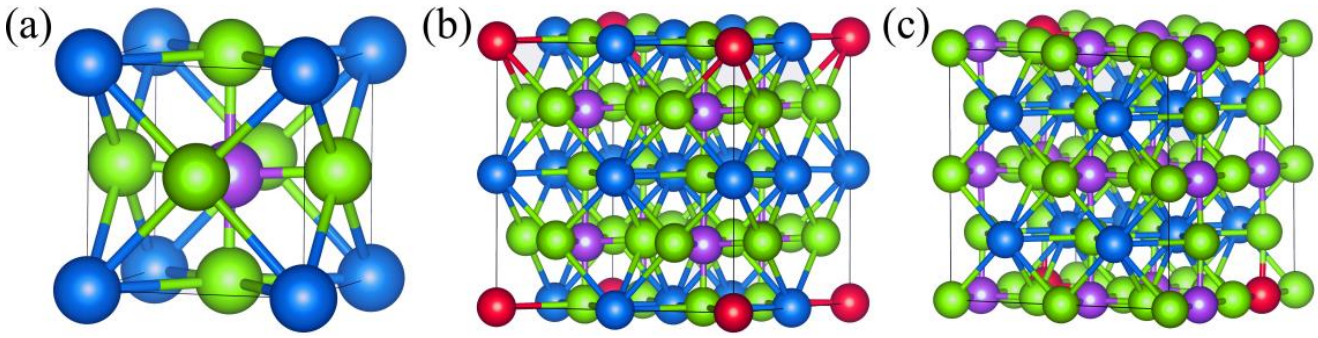

Figure 1. Crystal structures of (**a**) pure $BaTiO_3$, (**b**) Ba site substitution, and (**c**) Ti site substitution. Ba is dark blue, Ti is purple, O is light green, and Ce is red.

3.2. Electronic Properties

The electronic band structure of pristine and Ce-doped $BaTiO_3$ is presented in Figure 2. The energy band gap of pristine $BaTiO_3$ reached 2.081 eV, which was in accordance with the theoretical work [32]. Moreover, the band gap was indirect in nature as the CBM was obtained at point Γ, and the VBM was obtained at point A. For Ce-doped $BaTiO_3$, it was evident that the substitution of Ce for the Ba site slightly decreased the band gap from 2.081 eV to 2.023 eV, whereas the band gap was significantly decreased from 2.081 eV to 1.789 eV when Ce replaced the Ti site. The reduction in band gap indicated easier inter- and intra-band jumps of electrons and increased electrical conductivity of the material, which was consistent with the experimental work [19]. The decrease in the band gap of Ce-doped $BaTiO_3$ was caused by the increase in bond lengths. Due to increases in interatomic distances, it resulted in tight binding of electrons in valence shells, which requires more energy for conversion into the conduction electrons [35].

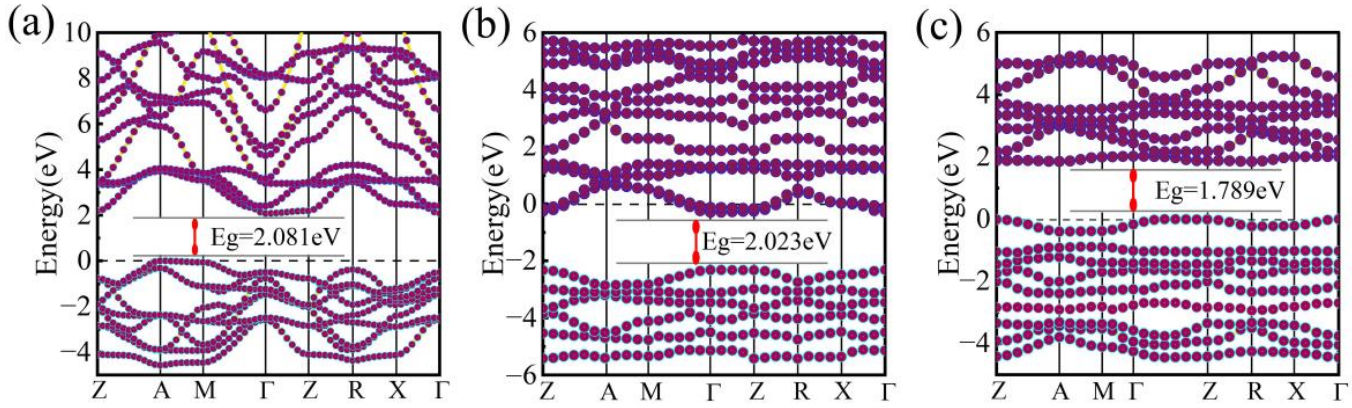

Figure 2. Electronic band structures of (**a**) pristine $BaTiO_3$, (**b**) Ba site doping, and (**c**) Ti site doping.

The substitution of the Ce element for the Ba site also induces the CBM and VBM to move to the smaller energy states and the transition of the band gap from indirect to direct, as the CBM and VBM are gained at the same point Γ. Moreover, the substitution of Ce for the Ba site results in the conduction band over the Fermi level and produces an impurity band. For Ce-doped at the Ti site, the process reduces the CBM compared to the pure perovskite, while the band gap is still indirect.

In order to further understand the mechanism of electronic structure, the total density of states (TDOS) and partial density of states (PDOS) of pristine and Ce-doped $BaTiO_3$ were computed at the optimized crystal structure, as shown in Figure 3. For pristine $BaTiO_3$, it can be observed that Ba has little contribution to the CBM and VBM. It just acts as a charge balancer to balance the system charge [36]. All unoccupied Ti 3d states are strongly hybridized with nearby O 2p states, and the CBM is mainly determined by the

unoccupied Ti 3d transition metal states. As a result, the band gap is attributed to the energy magnitude of Ti 3d and O 2p states. For Ce-doped $BaTiO_3$, as shown in Figure 3b,c, the main characteristics of CBM and VBM are consistent with pure $BaTiO_3$. The VBM is still mainly hybridized by the Ti 3d and O 2p states, and the CBM is determined by the Ti 3d states and the presence of the Ce 5d and 4f states. The substitution of Ba, which results in the presence of impurity bands in the conduction band, is attributed to the metallization of the crystal structure.

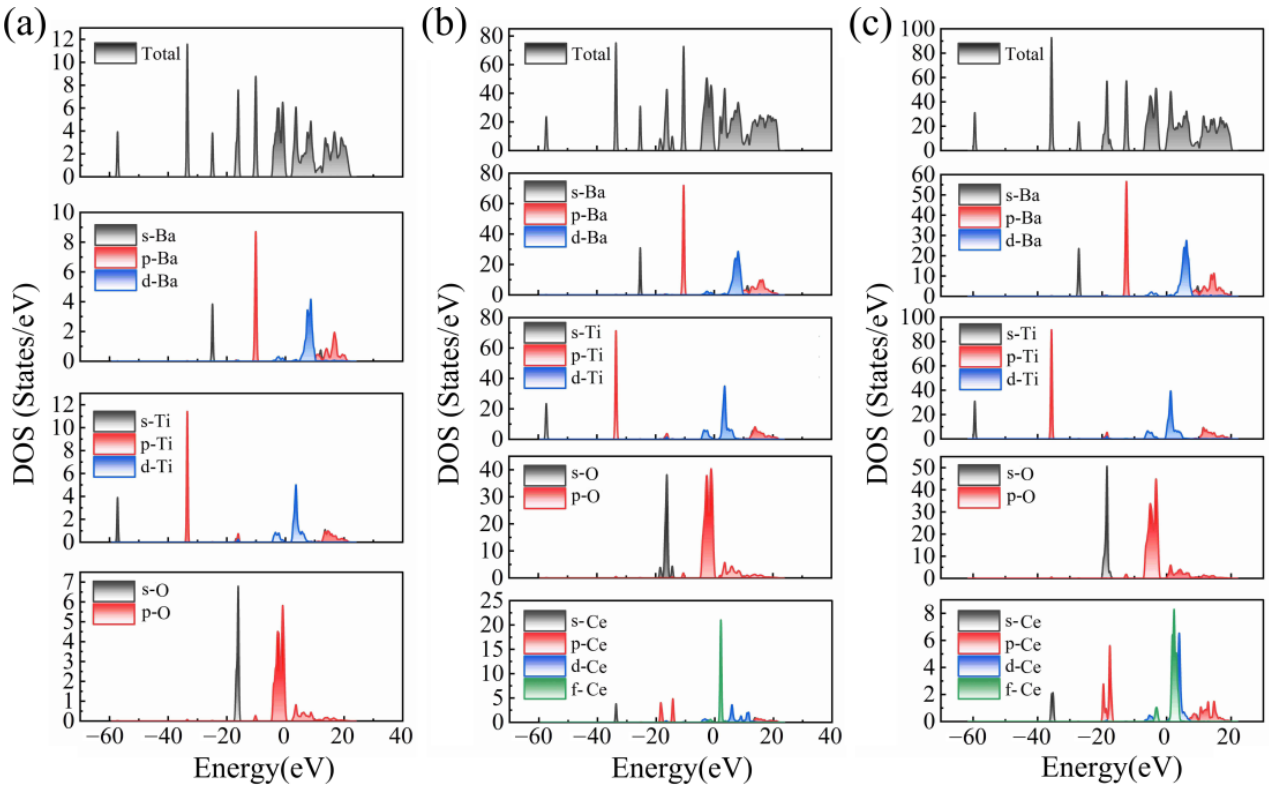

Figure 3. The total density of states and partial density of states of (**a**) $BaTiO_3$, (**b**) Ba site substitution, and (**c**) Ti site substitution.

For insight into the nature of chemical bonds before and after doping, the charge density distribution maps of pure and Ce-doped $BaTiO_3$ along the (0 0 1) plane have been calculated, respectively. As shown in Figure 4, in the presence of O 2p and Ti 3d hybrid states, Ti and O atoms form weak covalent bonds, whereas the Ba-O bond shows an ionic bond nature. When Ce was doped into the Ba and Ti sites, the nature of the ionic and weak covalent bonds between Ce and O was observed, respectively.

In addition, as presented in Table S1, the Mulliken charges of pure and Ce-doped $BaTiO_3$ were computed to quantify the number of charges transferred between atoms. It is a necessary complement to the electron charge density maps of Figure 4. The charge spilling of the materials was pretty low, which indicated that the basis set could well represent the structural properties of electrons [37]. For pristine $BaTiO_3$, both Ba and Ti atoms exhibit an electron loss, while the O atom is the opposite, indicating some electrons have transferred to the O atom to form ionic bonding. The amount of charge transferred from the O atom to the Ba atom and Ti atom is 1.44 and 0.74, respectively, which means that the ionic bond nature of the Ba-O bond is greater than the Ti-O bond. As for Ce-doped $BaTiO_3$, the Mulliken charge of the Ce atom is 1.55 and 0.92 for Ba site substitution and Ti site substitution, respectively, while the charge transfer from Ba and Ti atoms to O atom change slightly compared to undoped. The overlap populations of pristine and Ce-doped $BaTiO_3$ are listed in Table S2. The positive population number indicates that there is a

covalent bonding between atoms, while the negative number shows that there is a mutually exclusive anti-bonding between atoms. In the case of the population equal to zero, it is considered to be an ideal ionic bonding, and the larger the population value, the stronger the effect of the bonds [38]. For pure $BaTiO_3$, there is no covalent bond between Ba and O atoms but only an ionic bond, and there is a weak covalent bond between Ti and O atoms. For $Ba_{0.875}Ce_{0.125}TiO_3$, except anti-bond, the population of Ba-O and Ti-O bonds range from 0.06 to 0.07 and 0 to 0.64, respectively. The results show that the doping of Ce at the Ba site has exerted weak covalent bond characteristics between Ba and O atoms and reduced the covalent bond strength between Ti and O atoms. Moreover, the population of the Ce-O bond almost all approximates zero, which indicates that the Ce-O bond has mainly an ionic band and weak covalent bond nature. In terms of $BaTi_{0.875}Ce_{0.125}O_3$, it can be concluded from the results that the doping of Ce at Ti site also exerted a weak Ti-O covalent bond and reduced the covalent bond strength of the Ti-O bond. The population of the Ce-O bond is significantly greater than Ce doping at the Ba site, which indicates that the Ce-O bond exhibits a strong covalent bond and weak ionic bond nature. The calculated results of Mulliken charges and overlap populations accord with the charge density map.

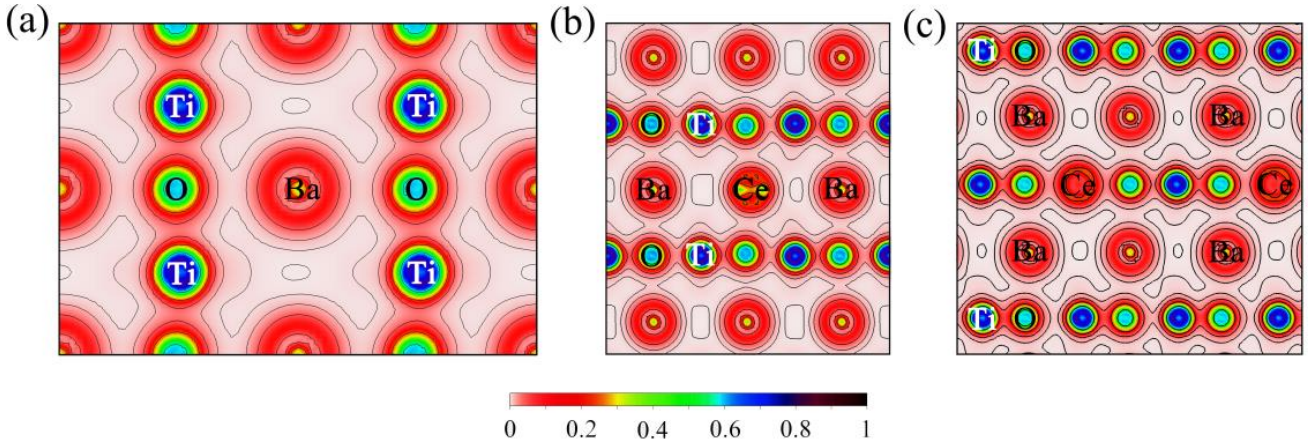

Figure 4. **C**harge density maps in the (0 0 1) plane for (**a**) pristine $BaTiO_3$, (**b**) Ba site substitution, and (**c**) Ti site substitution.

3.3. Optical Properties

In order to investigate the optical properties of the materials, the dielectric function, reflectivity, absorption, refractive index, and loss function were calculated. The optical properties are all functions of frequency or photon energy, and all the properties of the medium were computed from the complex dielectric function given as:

$$\varepsilon(\omega) = \varepsilon_R(\omega) + i\varepsilon_I(\omega) \tag{2}$$

where $\varepsilon_R(\omega)$ and $\varepsilon_I(\omega)$ represent the real and imaginary parts of the complex dielectric function, respectively. The imaginary part is related to momentum matrix elements. If the imaginary part $\varepsilon_I(\omega)$ of the dielectric function is known, the real part $\varepsilon_R(\omega)$ can be obtained via the Krammers–Kroning relations [39]. Furthermore, other optical parameters can also be calculated by the concerned formulas. The relations of all optical parameters such as refractive index $n(\omega)$, extinction coefficient $k(\omega)$, absorption coefficient $\alpha(\omega)$, reflectivity $R(\omega)$ and energy loss function $L(\omega)$ are shown as follows [40,41]:

$$\varepsilon_1(\omega) = 1 + \frac{2}{\pi}\rho_0 \int_0^\infty \frac{\omega' \varepsilon_2(\omega)}{\omega'^2 - \omega^2} d\omega \tag{3}$$

$$\varepsilon_2(\omega) = \frac{C}{\omega^2} \sum_{c,v} \int_{BZ} \frac{2}{(2\pi)^3} |M_{c,v}(k)|^2 \bullet \delta\left(E_c^k - E_v^k - \hbar\omega\right) d^3k \tag{4}$$

$$n(\omega) = \frac{\left[\varepsilon_1(\omega) + \sqrt{(\varepsilon_1(\omega))^2 + (\varepsilon_2(\omega))^2}\right]^{1/2}}{\sqrt{2}} \quad (5)$$

$$K(\omega) = \sqrt{\frac{\left[\sqrt{(\varepsilon_1(\omega))^2 + (\varepsilon_2(\omega))^2} - \varepsilon_1(\omega)\right]}{2}} \quad (6)$$

$$\alpha(\omega) = \sqrt{2}\omega\left[\sqrt{\varepsilon_1(\omega) + (\varepsilon_2(\omega))^2} - \varepsilon_1(\omega)\right]^{1/2} \quad (7)$$

$$L(\omega) = \frac{\varepsilon_2(\omega)}{(\varepsilon_1(\omega))^2 + (\varepsilon_2(\omega))^2} \quad (8)$$

$$R(\omega) = \frac{[n(\omega) - 1]^2 + [k(\omega)]^2}{[n(\omega) + 1]^2 + [k(\omega)]^2} \quad (9)$$

where subscripts c, v, and BZ represent the conduction band, valence band, and first Brillouin zone, respectively. $|M_{c,v}(k)|^2$ is the momentum matrix element, k is the reciprocal lattice vector, C is constant, ω is the angular frequency, E_v^k and E_c^k are intrinsic energy levels. The generation of the spectrum is related to the electron transition between energy levels, and the above formula lays a theoretical foundation for the calculation of band structure and optical properties.

The tetragonal structure has different lattice parameters along two directions, inducing different optical properties. For the comparison of the optical spectra changes in different lattice parameter directions, the optical parameters of all the materials along the x- and z-axis were calculated in this work. The values of the real and imaginary parts of the dielectric function along the x- and z-directions are shown in Figure 5. The static dielectric constants (ε_0) can be gained when the photon energies of the real part are equal to zero. As presented in Figure 5a, the static dielectric constant (ε_0) of pristine $BaTiO_3$ is recorded as 6.09 and 5.83 along the x- and z-axis, respectively, which was consistent with the previous theoretical works [42]. In addition, for $Ba_{0.875}TiCe_{0.125}O_3$, the value of ε_0 are recorded as 8.38 along the x-direction and 7.00 along the z-direction. In terms of $BaTi_{0.875}Ce_{0.125}O_3$, the static dielectric constants along the x-axis and z-axis are 5.911 and 5.709, respectively. As a result, it can be concluded that the substitution of Ce for the Ba site increased the static dielectric constant. In contrast, the static dielectric constant decreased at both the x-axis and z-axis when Ce was doped into the Ti site. The value of ε_0 represents the magnitude of the electronic polarization features of optical materials. The electron polarizability was improved significantly in terms of Ce doping at Ba sites, whereas the Ti site doping was the opposite. Moreover, ε_R achieved the maximum in the lower part of the photon energies at approximately 3.11, 3.32, and 3.15 eV for pristine $BaTiO_3$, Ba site substitution, and Ti site substitution, respectively, whereas the dispersion of ε_R decreased abruptly with the photon energies continuously increasing and obtained negative values. The positive and negative values of ε_R depicted the dielectric and metallic behaviors of the materials [43].

The peaks of the imaginary part $\varepsilon_I(\omega)$ are related to the band structure, representing the electron transition between the occupied states in the valence band and the unoccupied states in the conduction band [44]. According to Figure 5b, the peaks that simultaneously emerge in the x- and z-axis for pure $BaTiO_3$ towards the lower photon energies are believed to be originated from the electron transitions across forbidden bands. It can be inferred from the band structure that the sharp peaks are contributed by the electron transition from VBM located at point A in the BZ to the CBM located at point Γ. In terms of the incorporation of the Ce element, as shown in Figure 5d,f, several peaks have also been observed in the dispersion at a lower photon energy range, which is mainly due to the optical transition between the occupied states in the VBM at the point Γ, R and the unoccupied states in the CBM at the point Γ, Z. In addition, as shown in Figure 5d, for the substitution of Ce for the Ba site, a slight peak can be seen along the x- and z-axis at a lower photon energy of 0.13 and

0.09, respectively. The peaks at the lower photon energy range are mainly due to the effect of the impurity band in the band structure. Several low-intensity peaks can be easily observed in the higher photon energy range. They are attributed to the electron transition from the low-energy valence band to the unoccupied states in the conduction band.

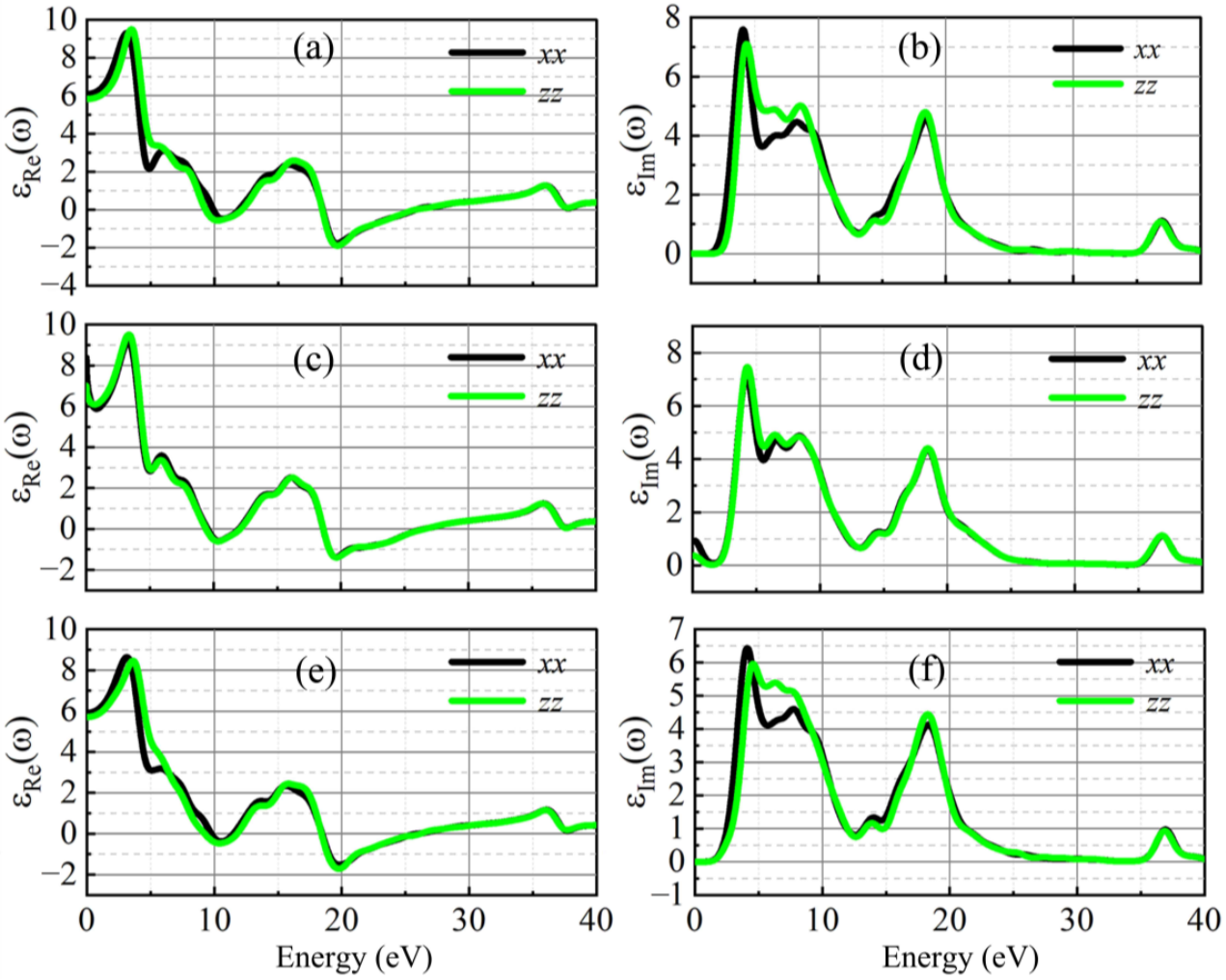

Figure 5. The real and imaginary parts of the dielectric function: (**a**,**b**) pure $BaTiO_3$, (**c**,**d**) $Ba_{0.875}TiCe_{0.125}O_3$, and (**e**,**f**) $BaTi_{0.875}Ce_{0.125}O_3$.

Figure 6 shows the absorption coefficient and reflectivity of these materials in different directions. As shown in Figure 6a,c,e, the incorporation of Ce slightly affects the absorption of incident light. Several moderate absorption peaks can be observed within the photon energy range of 0–15 eV. The absorption peaks of all the investigated materials are significantly enhanced with the photon energy increased continuously in the ultraviolet range. Although the lattice parameters show anisotropy in the x- and z-axis, all perovskites obtain almost identical absorption spectra along different directions. For pure $BaTiO_3$, the maximum absorption coefficient approaches 5.10×10^5 cm^{-1} at 19.26 eV and 5.20×10^5 cm^{-1} at 19.20 eV in the x- and z-axis, respectively. The maximum absorption coefficient of $Ba_{0.875}Ce_{0.125}TiO_3$ reaches 4.80×10^5 cm^{-1} at 19.23 eV in the x-axis and 4.82×10^5 cm^{-1} at 19.23 eV along the z-directions, respectively. In addition, there is a small absorption peak within the range of 3–6 eV, which is consistent with the experimental results [45,46]. In terms of $BaTi_{0.875}Ce_{0.125}O_3$, the maximum absorption coefficient closes to 4.78×10^5 cm^{-1} at 19.29 eV. Figure 6b,d,f illustrate the reflectivity of the materials. For the pristine and the substitution of Ce for the Ti site, the materials exhibit a slight difference in the x- and z-axis, whereas the reflectivity is almost identical in both directions for the substitution of

Ce for the Ba site. The intensity of reflection along the z-axis is stronger than that in the x-axis for all materials in the ultraviolet range of 5–10 eV. Several moderate reflection peaks can be observed in the low ultraviolet range (below 15 eV), whereas all materials show the strongest reflection peaks within the photon energy range of 15–20 eV. In addition, the maximum reflection of $BaTiO_3$ reaches 0.58 at 25.10 eV on the x-axis and 0.59 at 24.69 eV on the z-axis, respectively. For the Ba site substitution, the maximum reflection in the x- and the z-axis is 0.55 at 24.78 eV and 0.56 at 24.78 eV, respectively. In the case of Ce doping at the Ti site, the maximum reflection approaches 0.46 at 20.84 eV and 0.48 at 20.47 eV, respectively. It can be concluded that both the Ba and Ti sites of Ce-doped $BaTiO_3$ can reduce the reflectivity of the material.

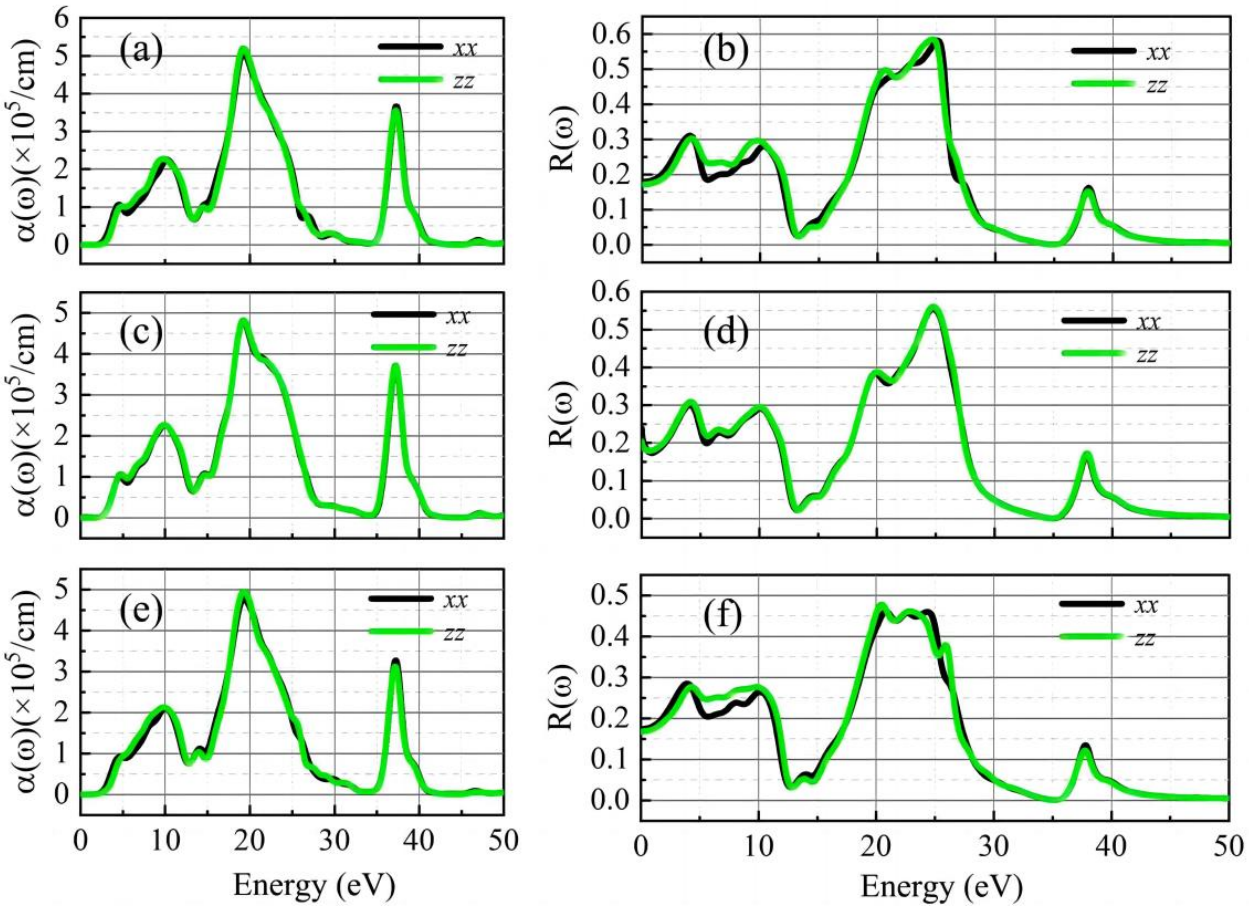

Figure 6. The absorption spectra (**a**,**c**,**e**) and reflectivity spectra (**b**,**d**,**f**) of the materials. The (**top**) represents pure $BaTiO_3$, the (**middle**) is $Ba_{0.875}TiCe_{0.125}O_3$, and the (**bottom**) is $BaTi_{0.875}Ce_{0.125}O_3$.

In addition, the refractive index and energy loss function (ELF) of the materials have been calculated to study the optical transparency and energy state of the electrons, respectively. As seen in Figure 7a,c,e, the refractive index of these materials in visible light and a large part of the low ultraviolet range are larger than one unity. The refractive index of the investigated materials decreases to less than one unity with the photon energy increase to the range of 10–13 eV as well as beyond 20 eV. Studies have shown that materials with a refractive index greater than or equal to one unity are transparent to incident light [47]. Therefore, it can be concluded that the materials are transparent to incident light when the photon energy is below 10 eV, and non-transparent in the ultraviolet range of 10–13 eV and beyond 20 eV. For pure $BaTiO_3$, the maximum refractive index is recorded as 3.11 at 3.27 eV at the x-axis and 3.14 at 3.64 eV at the z-axis. For Ce doping at the Ba site, the maximum refractive index approaches 3.09 at 3.44 eV at the x-axis and 3.14 at 3.53 eV at the z-axis. In the case of Ti site doping, the calculated maximum refractive index along

the x- and z-directions is the same, which is recorded as 2.99 at 3.27 eV. The energy loss function (ELF) represents the energy loss process of rapidly moving electrons passing through the materials, attributed to the plasmon resonance due to oscillations of valence electrons. As shown by peaks in Figure 7b,d,f. The energy of the maximum peaks occurs at $\varepsilon_I\ (\omega) < 1$ and $\varepsilon_R\ (\omega)$ is zero, which is generally recorded as the volume plasma frequency ω_p. For pure $BaTiO_3$, the plasma frequency values (ω_p) along the x- and z-axes is estimated to be 25.79 eV and 25.67 eV, respectively. In terms of the doping of Ce at the Ba site, the ω_p is almost the same along different directions, which is recorded as 26.71 eV. For Ti site doping, the ω_p is recorded as 26.50 eV and 26.3 eV in the x- and z-directions, respectively.

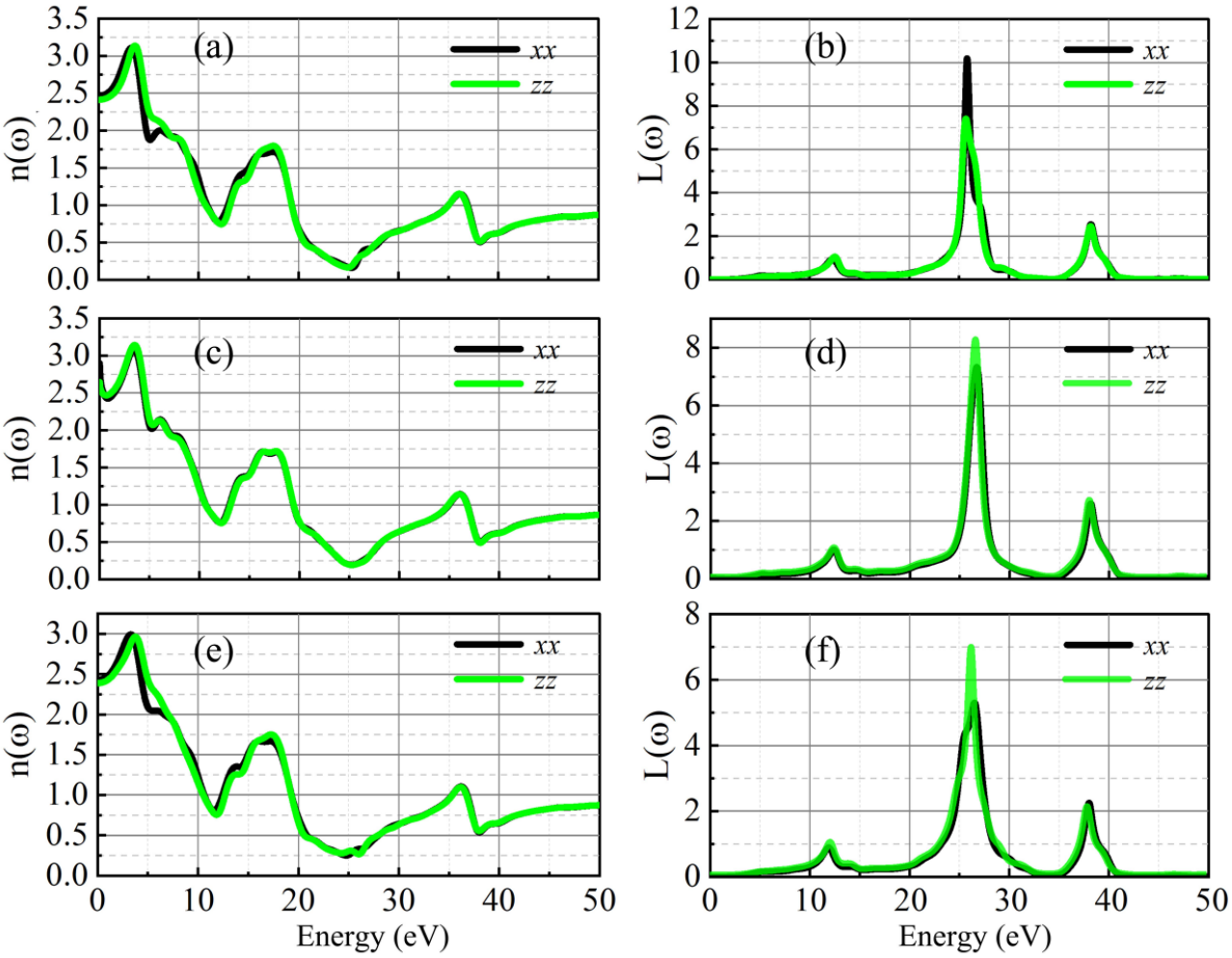

Figure 7. The refraction spectra (**a**,**c**,**e**) and energy loss function (ELF) (**b**,**d**,**f**) of $BaTiO_3$ (**top**), $Ba_{0.875}Ce_{0.125}$ TiO_3 (**middle**), and $BaTi_{0.875}Ce_{0.125}O_3$ (**bottom**).

4. Conclusions

The structural, electronic, and optical performance of pure $BaTiO_3$ and Ce substitution for different lattice sites were investigated based on first-principle calculation. It is found that the substitution of Ce for different sites leads to significant lattice distortion and a significant increase in the bond lengths of Ti-O and Ba-O. The substitution of Ce for the Ba site causes CBM and VBM to move to a smaller energy state, reducing the band gap and inducing the band gap shift from an indirect to a direct band gap. For Ti site doping, the process lowers CBM and reduces the band gap, whereas the band gap remains indirect. For pristine $BaTiO_3$, there is no covalent bond between Ba and O atoms but an ionic bond, while there is a weak covalent bond between Ti and O atoms. The doping of Ce at the Ba site exerts mainly an ionic band and weak covalent bond nature between Ce and O atoms.

In the case of Ti site doping, the Ce-O bond exhibits a strong covalent bond and weak ionic bond nature. The substitution of Ce for the Ba site increases the static dielectric constant, whereas it decreases when Ce is doped into the Ti site. In addition, the substitution of Ce for different sites reduces the reflectivity of the material, while the transparency of the materials before and after doping is almost the same. The materials are transparent to incident light when the photon energy is below 10 eV, whereas opacity is in the ultraviolet range of 10–13 eV and beyond 20 eV. This study provides a new theoretical basis for exploring the different properties of the $BaTiO_3$-based system.

Supplementary Materials: The following supporting information can be downloaded at: https://www.mdpi.com/article/10.3390/cryst13020255/s1, Table S1: Atomic Mulliken charges populations of pure and Ce-doped $BaTiO_3$. Table S2: Bond overlap populations of pure and Ce-doped $BaTiO_3$.

Author Contributions: Conceptualization, H.Y. and K.G.; Data curation, I.T.; Formal analysis, Z.L., B.X., and P.M.; Investigation, J.L.; Methodology, H.Y.; Resources, F.E.H.T. and K.Y.; Software, K.F.; Supervision, K.G.; Validation, T.C. and Q.J.; Writing—original draft, H.Y.; Writing—review and editing, K.G., K.Y. All authors have read and agreed to the published version of the manuscript.

Funding: This research was funded by the National Natural Science Foundation of China (Grant No. 52002164), and the Natural Science Foundation of Jiangxi Province of China (Grant No. 20202BABL204013).

Data Availability Statement: The data presented in this study are available on request.

Conflicts of Interest: The authors declare no conflict of interest.

References

1. Akedo, J. Room Temperature Impact Consolidation (RTIC) of Fine Ceramic Powder by Aerosol Deposition Method and Applications to Microdevices. *J. Therm. Spray Technol.* **2008**, *17*, 181–198. [CrossRef]
2. Choi, J.J.; Hahn, B.D.; Ryu, J.; Yoon, W.H.; Lee, B.K.; Park, D.S. Preparation and characterization of piezoelectric ceramic–polymer composite thick films by aerosol deposition for sensor application. *Sens. Actuators A* **2009**, *153*, 89–95. [CrossRef]
3. Koruza, J.; Bell, A.J.; Froemling, T.; Webber, K.G.; Wang, K.; Rödel, J. Requirements for the transfer of lead-free piezoceramics into application. *J. Mater.* **2018**, *4*, 13–26. [CrossRef]
4. Lee, G.J.; Kim, B.H.; Yang, S.A.; Park, J.J.; Bu, S.D.; Lee, M.K. Piezoelectric and ferroelectric properties of (Bi, Na)TiO_3-(Bi, Li)TiO_3-(Bi, K)TiO_3 ceramics for accelerometer application. *J. Am. Ceram. Soc.* **2017**, *100*, 678–685. [CrossRef]
5. Rödel, J.; Li, J.F. Lead-free piezoceramics: Status and perspectives. *MRS Bull.* **2018**, *43*, 576–580. [CrossRef]
6. Shibata, K.; Wang, R.; Tou, T.; Koruza, J. Applications of lead-free piezoelectric materials. *MRS Bull.* **2018**, *43*, 612–616. [CrossRef]
7. Zhao, Q.; Yang, L.; Ma, Y.; Huang, H.; He, H.; Ji, H.; Qiu, J. Highly sensitive, reliable and flexible pressure sensor based on piezoelectric PVDF hybrid film using MXene nanosheet reinforcement. *J. Alloys Compd.* **2021**, *886*, 161069. [CrossRef]
8. Itoh, K.; Zeng, L.Z.; Nakamura, E.; Mishima, N. Crystal structure of $BaTiO_3$ in the cubic phase. *Ferroelectrics* **1985**, *63*, 29–37. [CrossRef]
9. Shrout, T.R.; Zhang, S.J. Lead-free piezoelectric ceramics: Alternatives for PZT? *J. Electroceram.* **2007**, *19*, 113–126. [CrossRef]
10. Wu, J.; Wu, W.; Xiao, D.; Wang, J.; Yang, Z.; Peng, Z.; Zhu, J. (Ba, Ca)(Ti, Zr)O_3-$BiFeO_3$ lead-free piezoelectric ceramics. *Curr. Appl. Phys.* **2012**, *12*, 534–538. [CrossRef]
11. Yang, W.G.; Zhang, B.P.; Ma, N.; Zhao, L. High piezoelectric properties of $BaTiO_3$-xLiF ceramics sintered at low temperatures. *J. Eur. Ceram. Soc.* **2012**, *32*, 899–904. [CrossRef]
12. Jaita, P.; Jarupoom, P. Enhanced electric field-induced strain and electrostrictive response of lead-free $BaTiO_3$-modified $Bi_{0.5}(Na_{0.80}K_{0.20})_{0.5}TiO_3$ piezoelectric ceramics. *J. Asian. Ceram. Soc.* **2021**, *9*, 975–987. [CrossRef]
13. Guo, X.; Wu, Y.; Zou, Y.; Wang, Z. Effects of addition of $BiFeO_3$ on phase transition and dielectric properties of $BaTiO_3$ ceramics. *J. Mater. Sci. Mater. Electron.* **2012**, *23*, 1072–1076. [CrossRef]
14. Li, Y.; Liao, Z.; Fang, F.; Wang, X.; Li, L.; Zhu, J. Significant increase of Curie temperature in nano-scale $BaTiO_3$. *Appl. Phys. Lett.* **2014**, *105*, 182901. [CrossRef]
15. Brajesh, K.; Ranjan, S.; Garg, A. Phase evolution and enhanced room temperature piezoelectric properties response of lead-free Ru doped $BaTiO_3$ ceramic. *arXiv* **2021**, arXiv:2112.14982.
16. Ben, L.; Sinclair, D.C. Anomalous Curie temperature behavior of A-site Gd-doped $BaTiO_3$ ceramics: The influence of strain. *Appl. Phys. Lett.* **2011**, *98*, 092907. [CrossRef]

17. Sareecha, N.; Shah, W.A.; Mirza, M.L.; Maqsood, A.; Awan, M.S. Electrical investigations of Bi-doped $BaTiO_3$ ceramics as a function of temperature. *Physica B Condens. Matter.* **2018**, *530*, 283–289. [CrossRef]
18. Cernea, M.; Monnereau, O.; Llewellyn, P.; Tortet, L.; Galassi, C. Sol–gel synthesis and characterization of Ce doped-$BaTiO_3$. *J. Eur. Ceram. Soc.* **2006**, *26*, 3241–3246. [CrossRef]
19. Hwang, J.H.; Han, Y.H. Electrical properties of cerium-doped $BaTiO_3$. *J. Am. Ceram. Soc.* **2001**, *84*, 1750–1754. [CrossRef]
20. Curecheriu, L.P.; Curecheriu, L.P.; Deluca, M.; Mocanu, Z.V.; Pop, M.V.; Nica, V.; Horchidan, N.; Mitoseriu, L. Investigation of the ferroelectric–relaxor crossover in Ce-doped $BaTiO_3$ ceramics by impedance spectroscopy and Raman study. *Phase Transit.* **2013**, *86*, 703–714. [CrossRef]
21. Vanderbilt, D. Soft self-consistent pseudopotentials in a generalized eigenvalue formalism. *Phys. Rev. B.* **1990**, *41*, 7895. [CrossRef] [PubMed]
22. Wang, Y.; Wang, Y.; Fullon, R.; Acerce, M.; Petoukhoff, C.E.; Yang, J.; Chen, C.; Chhowalla, M. Solution-processed MoS2/organolead trihalide perovskite photodetectors. *Adv. Mater.* **2017**, *29*, 1603995. [CrossRef] [PubMed]
23. Rizwan, M.; Rizwan, M.; Shahid, A.; Mahmood, T.; Zafar, A.A.; Aslam, I.; Adnan, N.; Cao, C.B. Effect of magnesium on structural and optical properties of $CaTiO_3$: A DFT study. *Phys. B* **2019**, *568*, 88–91. [CrossRef]
24. Perdew, J.P.; Wang, Y. Accurate and simple analytic representation of the electron-gas correlation energy. *Phys. Rev. B* **1992**, *45*, 13244. [CrossRef] [PubMed]
25. Nolan, M.; Grigoleit, S.; Sayle, D.C.; Parker, S.C.; Watson, G.W. Density functional theory studies of the structure and electronic structure of pure and defective low index surfaces of ceria. *Surf. Sci.* **2005**, *576*, 217–229. [CrossRef]
26. Ali, A.; Khan, I.; Ali, Z.; Khan, F.; Ahmad, I. First-principles study of $BiFeO_3$ and $BaTiO_3$ in tetragonal structure. *Int. J. Mod. Phys. B* **2019**, *33*, 1950231. [CrossRef]
27. German, E.; Faccio, R.; Mombrú, A.W. A DFT+ U study on structural, electronic, vibrational and thermodynamic properties of TiO_2 polymorphs and hydrogen titanate: Tuning the Hubbard 'U-term'. *J. Phys. Commun.* **2017**, *1*, 055006. [CrossRef]
28. Castleton, C.; Kullgren, J.; Hermansson, K. Tuning LDA+U for electron localization and structure at oxygen vacancies in ceria. *J. Chem. Phys.* **2007**, *127*, 244704. [CrossRef]
29. Upadhyay, S.; Upadhyay, S.; Shrivastava, J.; Solanki, A.; Choudhary, S.; Sharma, V.; Kumar, P.; Dass, S. Enhanced photoelectrochemical response of $BaTiO_3$ with Fe doping: Experiments and first-principles analysis. *J. Phys. Chem. C* **2011**, *115*, 24373–24380. [CrossRef]
30. Xie, P.; Xie, P.; Yang, F.; Li, R.; Ai, C.; Lin, C.; Lin, S. Improving hydrogen evolution activity of perovskite $BaTiO_3$ with Mo doping: Experiments and first-principles analysis. *Int. J. Hydrog. Energy.* **2019**, *44*, 11695–11704. [CrossRef]
31. Raengthon, N.; McCue, C.; Cann, D.P. Relationship between tolerance factor and temperature coefficient of permittivity of temperature-stable high permittivity $BaTiO_3$-$Bi(Me)O_3$ compounds. *J. Adv. Dielectr.* **2016**, *6*, 1650002. [CrossRef]
32. Evarestov, R.A.; Bandura, A.V. First-principles calculations on the four phases of $BaTiO_3$. *J. Comput. Chem.* **2012**, *33*, 1123–1130. [CrossRef] [PubMed]
33. Zhang, H.Y.; Zeng, Z.Y.; Zhao, Y.Q.; Lu, Q.; Cheng, Y. First-principles study of lattice dynamics, structural phase transition, and thermodynamic properties of barium titanate. *Z. Naturforsch A* **2016**, *71*, 759–768. [CrossRef]
34. Aoyagi, S.; Kuroiwa, Y.; Sawada, A.; Yamashita, I.; Atake, T. Composite structure of $BaTiO_3$ nanoparticle investigated by SR X-ray diffraction. *J. Phys. Soc. Jpn.* **2002**, *71*, 1218–1221. [CrossRef]
35. Rizwan, M.; Ayub, A.; Shakil, M.; Usman, Z.; Gillani, S.S.A.; Jin, H.B.; Cao, C.B. Putting DFT to trial: For the exploration to correlate structural, electronic and optical properties of M-doped (M = Group I, II, III, XII, XVI) lead free high piezoelectric c-$BiAlO_3$. *J. Mater. Sci. Eng. B* **2021**, *264*, 114959. [CrossRef]
36. Ching-Prado, E. Stress dependence of structure, electronic and optical properties of $BaTiO_3$ from WC, VdW-DF-C09 and HSE functional calculations. *Ferroelectrics* **2018**, *535*, 171–182. [CrossRef]
37. Zhang, X.; Luo, X.; Han, J.; Li, J.; Han, W. Electronic structure, elasticity and hardness of diborides of zirconium and hafnium: First principles calculations. *Comput. Mater. Sci.* **2008**, *44*, 411–421. [CrossRef]
38. Mulliken, R.S. Electronic population analysis on LCAO–MO molecular wave functions. II. Overlap populations, bond orders, and covalent bond energies. *J. Chem. Phys.* **1955**, *23*, 1841–1846. [CrossRef]
39. Laksari, S.; Chahed, A.; Abbouni, N.; Benhelal, O.; Abbar, B. First-principles calculations of the structural, electronic and optical properties of $CuGaS_2$ and $AgGaS_2$. *Comput. Mater. Sci.* **2006**, *38*, 223–230. [CrossRef]
40. Sheng, X.C. *The Spectrum and Optical Property of Semiconductor*, 1st ed.; Science Press: Beijing, China, 1992; p. 24.
41. Garcia, J.C.; Scolfaro, L.M.R.; Lino, A.T.; Freire, V.N.; Farias, G.A.; Silva, C.C.; da Silva, E.F., Jr. Structural, electronic, and optical properties of ZrO_2 from ab initio calculations. *J. Appl. Phys.* **2006**, *100*, 104103. [CrossRef]
42. Chik, A.; Adewale, A.A.; Pa, F.C. Influence of calcium and zirconium as codopant on electronic and optical properties of $BaTiO_3$ using first principle calculation. *AIP Conf. Proc.* **2021**, *2339*, 020217.
43. Alshoaibi, A.; Kanoun, M.B.; Ul Haq, B.; AlFaify, S.; Goumri-Said, S. Insights into the Impact of Yttrium Doping at the Ba and Ti Sites of $BaTiO_3$ on the Electronic Structures and Optical Properties: A First-Principles Study. *ACS Omega* **2020**, *5*, 15502–15509. [CrossRef] [PubMed]
44. Liu, X.; Fan, H.Q. Theoretical studies on electronic structure and optical properties of Bi_2WO_6. *Optik* **2018**, *158*, 962–969. [CrossRef]

45. Hafid, L.; Godefroy, G.; El Idrissi, A.; Michel-Calendini, F. Absorption spectrum in the near UV and electronic structure of pure barium titanate. *Solid State Commun.* **1988**, *66*, 841–845. [CrossRef]
46. Chernova, E.; Pacherova, O.; Chvostova, D.; Dejneka, A.; Kocourek, T.; Jelinek, M.; Tyunina, M. Strain–controlled optical absorption in epitaxial ferroelectric $BaTiO_3$ films. *Appl. Phys. Lett.* **2015**, *106*, 192903. [CrossRef]
47. Arbab, A.I. On the refractive index and photon mass. *Optik* **2016**, *127*, 6682–6687. [CrossRef]